Geophysical Journal International

Geophys. J. Int. (2024) **238,** 1137–1149
Advance Access publication 2024 June 12
GJI Geodynamics and Tectonics

https://doi.org/10.1093/gji/ggae203

Effects of using the consistent boundary flux method on dynamic topography estimates

Karen Williams,[1] D. Sarah Stamps,[1] Jaqueline Austermann,[2] Scott King[1] and Emmanuel Njinju[1,3]

[1]*Department of Geosciences, Virginia Tech,* 4044 *Derring Hall,* 926 *West Campus Drive, Blacksburg, VA* 24061*, USA. E-mail:* karenw@vt.edu ,
[2]*Department of Earth and Environmental Sciences, Columbia University, Lamont-Doherty Earth Observatory, Seismology Bldg., Room* 223*,* 61 *Route* 9 *W, Palisades, NY* 10964-8000*, USA*
[3]*Department of Earth and Planetary Science, University of California, Davis,* 462 *Crocker Lane, Davis, CA* 95616*, USA*

Accepted 2024 May 24. Received 2024 May 16; in original form 2023 June 10

SUMMARY

Dynamic topography is defined as the deflection of Earth's surface due to the convecting mantle. ASPECT (Advanced Solver for Planetary Evolution, Convection, and Tectonics) is a continually evolving, finite element code that uses modern numerical methods to investigate problems in mantle convection. With ASPECT version 2.0.0 a consistent boundary flux (CBF) algorithm, used to calculate radial stresses at the model boundaries, was implemented into the released version of ASPECT. It has been shown that the CBF algorithm improves the accuracy of dynamic topography calculations by approximately one order of magnitude. We aim to evaluate the influence of the CBF algorithm and explore the geophysical implications of these improved estimates of dynamic topography changes along the East Coast of the United States. We constrain our initial temperature conditions using the tomography models SAVANI, S40RTS and TX2008, and combine them with a corresponding radial viscosity profile (2 for TX2008) and two different boundary conditions for a total of eight experiments. We perform simulations with and without the CBF method, which takes place during post-processing and does not affect the velocity solution. Our dynamic topography calculations are spatially consistent in both approaches, but generally indicate an increase in magnitude using the CBF method (on average ∼15 and ∼76 per cent absolute change in present-day instantaneous and rate of change of dynamic topography, respectively). This enhanced accuracy in dynamic topography calculations can be used to better evaluate the effects of mantle convection on surface processes including vertical land motions, sea level changes, and sedimentation and erosion. We explore results along the US East Coast, where a Pliocene shoreline has been deformed by dynamic topography change. An increased accuracy in estimates of dynamic topography can improve Pleistocene and Pliocene sea level reconstructions, which allow for a better understanding of past sea level changes and ice sheet stability.

Key words: Numerical modelling; Dynamics of lithosphere and mantle; Mantle processes.

1 INTRODUCTION

Mantle convection driven by heterogeneities in the density structure causes radial stresses at Earth's surface, which result in the deformation of Earth's topography. A hot, low-density anomaly in the mantle will rise resulting in dynamic uplift and a cold, high-density anomaly will sink resulting in dynamic subsidence. The amplitude and wavelength of dynamic topography is in proportion to the intensity, timescale and depth of mantle flow. Though the theory of dynamic topography has been well-established, there remain discussions about what components of mantle density and flow should be included in the definition of dynamic topography signal (i.e. Molnar *et al.* 2015; Forte & Rowley 2022). Further, the accuracy and precision of dynamic topography predictions are hampered by uncertainties in Earth's density field (including compositional changes) and rheology (Panasyuk & Hager 2000). As a result of these differences in definition and uncertainties in input, proposed present-day dynamic topography amplitude estimates range from a few hundred to over 3000 m (Flament *et al.* 2013; Molnar *et al.* 2015). Dynamic topography changes have implications for a number of surface processes and have been studied extensively to analyse surface subsidence and uplift (e.g. Bertelloni & Gurnis 1997; Liu 2015; Muller *et al.* 2018), ice sheet stability and global sea level changes (e.g. Gurnis 1990; Moucha *et al.* 2008; Conrad &

Husson 2009; Austermann *et al.* 2015), landscape evolution (Hack 1975; Ruetenik *et al.* 2016; Moucha & Ruetenik 2017; Hoggard *et al.* 2021) and sedimentation and erosion (Heine *et al.* 2008; Liu 2014; Ding *et al.* 2019). Enhanced accuracy in dynamic topography calculations can be used to better evaluate the effects of mantle convection on these surface processes.

Various approaches have been used to calculate dynamic topography, including free surface calculations (e.g. Gurnis *et al.* 1996; Zhong *et al.* 1996; Kramer *et al.* 2012) and the 'sticky air' method (e.g. Crameri *et al.* 2012), but the most common approach computes dynamic topography as compensation heights of radial stresses at the surface (e.g. McKenzie 1977; Hager *et al.* 1985; Zhong *et al.* 1993). Mantle convection produces variability in pressure and stress in the mantle. These stresses transfer tractions to the Moho, which will deform to balance out the normal force, thus resulting in surface topography. In analytical and numerical models of mantle convection, the Earth's mantle is treated as a viscous fluid where the degree of buoyancy in the mantle determines the flow, pressure and radial stresses for computing dynamic topography. In the past decades, significant progress has been made in developing mantle convection models in the 3-D spherical domain (e.g. Baumgardner 1985; Tackley 1993; Bunge *et al.* 1996; Ratcliff *et al.* 1996; Zhong *et al.* 2000; Yoshida & Kageyama 2004; Stemmer *et al.* 2006; Choblet *et al.* 2007). In computer simulations, the development of software and computational methods has advanced mantle convection models from simple 2-D meshes using fixed-point linear solvers to complex 3-D discretizations with adaptively refined finite element non-linear solvers. These advances open up possibilities to more accurately simulate global mantle convection to solve realistic problems using compressible flow with complex geometries.

ASPECT (Advanced Solver for Planetary Evolution, Convection, and Tectonics; Kronbichler *et al.* 2012; Bangerth *et al.* 2020) is a continually evolving, finite element code that uses modern numerical methods to investigate problems in mantle convection and lithospheric deformation. ASPECT's capabilities stand apart from other mantle convection codes for a number of reasons, including, (1) governing equations that are dimensional for computing high-Rayleigh number flows allowing both incompressible and compressible flow, (2) an adaptive mesh refinement to perform mesh adaptation spatially and temporally, (3) effective linear and non-linear solvers to handle significant heterogeneities and large, complex systems and (4) accurate discretization and stabilization methods based on high-order finite elements, which leads to higher accuracy and reliability with fewer unknowns. In ASPECT, dynamic topography is computed through a stress-balancing approach assuming the radial stress at the surface is balanced by excess or deficit topography. With the release of ASPECT version 2.0.0, a consistent boundary flux (CBF) method to calculate radial stresses at the surface was implemented, which has been shown to significantly improve dynamic topography estimates (Zhong *et al.* 1993; Liu & King 2019). Formulation and validation of the CBF method for computing radial stress to calculate dynamic topography is discussed in Section 2.

In this work, we define dynamic topography as vertical surface deflections induced by surface stresses. It is important to note that our definition of dynamic topography includes the whole mantle, including the lithospheric mantle (i.e. Forte & Rowley 2022). Dynamic topography is computed by balancing radial stresses at the Earth's surface. We follow a similar dynamic topography modelling approach used in Austermann *et al.* (2017), who calculate the change in dynamic topography to compare surface deflections with global sea level markers during the last interglacial (LIG) period (∼125 ka). Austermann *et al.* (2017) concluded that changes in dynamic topography are strongly correlated with sea level markers suggesting that a prominent signal of dynamic topography was present during the LIG and should be accounted for in studies determining global sea level during the LIG. Our aim in this study is to assess the influence of the CBF method and analyse some potential geophysical implications of the improved estimates for instantaneous present-day and rate of change of dynamic topography solutions on the US East Coast.

2 METHODS

2.1 Dynamic topography modelling

We use ASPECT version 2.2.0 to model dynamic topography. ASPECT solves the conservation equations in a 3-D domain driven by variations in density due to temperature distributions in the mantle. Section 2.1.1 lays out the general formulation of the compressible Stokes system used in our models. However, it should be noted that ASPECT offers various methods for approximation, particularly with compressible flow, which may alter the derivation. Methods for constructing the compressible Stokes system described below are well-documented in the literature (e.g. Leng & Zhong 2008; Dannberg & Heister 2016; Heister *et al.* 2017; Gassmöller *et al.* 2020). Section 2.1.2 describes the basic formulation of the CBF method to determine surface radial stresses for computing dynamic topography. Validation that the CBF method improves dynamic topography estimates is also discussed in this section. The CBF method was originally developed by Zhong *et al.* (1993) and has been implemented into other mantle convection codes including CitcomS (Zhong *et al.* 2008) and Rhea (Burstedde *et al.* 2013).

2.1.1 Formulation of the compressible Stokes system

Assuming a compressible fluid, the governing equations are:

$$-\nabla\cdot[2\eta\left(\epsilon\,(\boldsymbol{u})-\frac{1}{3}\,(\nabla\cdot\boldsymbol{u})\,1\right]+\nabla p\;=\rho\boldsymbol{g} \tag{1}$$

$$\nabla\cdot\;(\rho\boldsymbol{u})=0 \tag{2}$$

$$\begin{aligned}&\rho C_p\left(\tfrac{\mathrm{d}T}{\mathrm{d}t}+\boldsymbol{u}\cdot\nabla T\right)-\nabla\cdot k\nabla T\;=\;\rho H\\&+2\eta\left(\epsilon\,(\boldsymbol{u})-\;\tfrac{1}{3}\,(\nabla\cdot\boldsymbol{u})\,1\right)\;:\left(\epsilon\,(\boldsymbol{u})-\;\tfrac{1}{3}\,(\nabla\cdot\boldsymbol{u})\,1\right)\\&+\alpha T\,(\boldsymbol{u}\cdot\nabla p)\\&+\rho T\Delta S\left(\tfrac{\mathrm{d}X}{\mathrm{d}t}+\boldsymbol{u}\cdot\nabla X\right),\end{aligned} \tag{3}$$

where eqs (1) and (2) are the momentum and the mass conservation equations, respectively. These constitute the compressible Stokes system where $\boldsymbol{u}=\boldsymbol{u}(\boldsymbol{x},t)$ is the velocity field, $p=p(\boldsymbol{x},t)$ is the pressure field, $\boldsymbol{\rho}=\boldsymbol{\rho}\;(\boldsymbol{x},\;t)$ is density, $\eta(\mathbf{x})$ is viscosity, $\boldsymbol{g}$ is the gravitational acceleration and $\epsilon(\boldsymbol{u})=\frac{1}{2}(\nabla\boldsymbol{u}+\nabla\boldsymbol{u}^T)$ is the strain rate. Eq. (3) describes the temperature field $T=T(\boldsymbol{x},t)$ containing terms for advection with flow velocity $\boldsymbol{u}$ and heat conduction. The right-hand side of eq. (3) corresponds to internal heat production, friction heating, adiabatic heating due to compression and latent heat produced or consumed during phase changes. C_p is the specific heat, and k is the thermal conductivity.

The finite element discretization requires the weak form of the momentum and mass conservation equations (eqs 1 and 2, respectively), which are obtained by multiplying eqs (1) and (2) by their respective test functions, integrating over the domain, Ω, and then integrating by parts.

The weak form of the discrete momentum equation reads

$$\left(2\eta\epsilon\left(\boldsymbol{u}_h^n\right),\ \ \epsilon\left(\boldsymbol{v}_i^u\right)\right)_\Omega - \frac{2}{3}\eta\left(\nabla\cdot\boldsymbol{u}_h^n,\ \ \nabla\cdot\boldsymbol{v}_i^u\right)_\Omega + \left(\nabla p_h^n,\ \ \boldsymbol{v}_i^u\right)_\Omega = \left(\rho\boldsymbol{g},\ \boldsymbol{v}_i^u\right)_\Omega, \tag{4}$$

where $\boldsymbol{u}_h^n(\boldsymbol{x}) = \sum_{j=1}^{N_u} U_j^n \boldsymbol{v}_j^u(\boldsymbol{x})$ and $p_h^n(\boldsymbol{x}) = \sum_{j=1}^{N_p} P_j^n \boldsymbol{v}_j^p(\boldsymbol{x})$ are the finite element approximations for velocity and pressure computed by determining coefficients, U_j^n and P_j^n**,** that match the polynomial degree of the finite element basis functions, $\boldsymbol{v}_j^u$ and $\boldsymbol{v}_j^p$, respectively. These approximations are inserted into eq. (1) and multiplied by velocity test function $\boldsymbol{v}_i^u$ at index i with $i = 1\ldots N_u$ and $i = 1\ldots N_p$. This forms the inner products denoted by (•,•), which compute tensors (first term), scalars (second term) and vectors (third term), resulting in scalar quantities for each term. All terms are integrated over the domain, Ω. The first two terms are further integrated by parts. We remove the finite element index notation for readability in the remainder of this description of the formulation so that eq. (4) reads

$$\left(2\eta\epsilon\left(\boldsymbol{u}\right), \epsilon\left(\boldsymbol{v}\right)\right) - \frac{2}{3}\eta\left(\nabla\cdot\boldsymbol{u}, \nabla\cdot\boldsymbol{v}\right) + \left(\nabla p, \boldsymbol{v}\right) = \left(\rho\boldsymbol{g}, \boldsymbol{v}\right). \tag{5}$$

Integrating by parts on the pressure term yields

$$\left(2\eta\epsilon\left(\boldsymbol{u}\right), \epsilon\left(\boldsymbol{v}\right)\right) - \left(\frac{2}{3}\eta\nabla\cdot\boldsymbol{u}, \nabla\cdot\boldsymbol{v}\right) - \left(p, \nabla\cdot\boldsymbol{v}\right) = \left(\rho\boldsymbol{g}, \boldsymbol{v}\right). \tag{6}$$

Eqs (5) and (6) are modified equations of the weak formulation based on Dannberg & Heister (2016), who include only material properties (not their derivatives) in the equations. For the momentum equation, integration by parts is done on the pressure term ($\boldsymbol{v} = 0$ on the boundary), which removes the boundary integral in eq. (6). The CBF post-processing method recovers the normal component of the boundary traction that was removed in eq. (6).

For compressible flow, the mass conservation equation must be linearized. This linearization is done by replacing eq. (2) with

$$\nabla\cdot\ \left(\rho^*\boldsymbol{u}\right) = 0, \tag{7}$$

where $\rho^* = \rho^*(z)$ is a prescribed density profile. Eq. (7) is linearized since ρ^* is spatially variable but no longer depends on the solution variables, velocity and pressure, whose quantities are currently being solved for. However, the product $\rho^*\boldsymbol{u}$ is not a finite element function. To make eq. (7) computable, the divergence is multiplied out:

$$\nabla\cdot\boldsymbol{u} + \frac{1}{\rho^*}\nabla\rho^*\cdot\boldsymbol{u} = 0. \tag{8}$$

Note that our approach for linearization is only one of many methods. Density in the continuity equation for compressible flow is expressed in terms of pressure and temperature ($\nabla\rho(p, T) = \frac{\partial\rho}{\partial p}\ \nabla p + \frac{\partial\rho}{\partial T}\ \nabla T$). The approximation, $\nabla p \approx \rho\boldsymbol{g}$, is made based on the theory that in general, pressure is only a function in L_2 (Ern & Guermond 2004; Heister *et al.* 2017). This means it is unlikely to obtain an approximation better than $||p - p_h||_{\mathrm{L}_2} = \mathcal{O}(h)$ for the finite element approximation of pressure, p_h. Using a term that contains ∇p in the equation for $\nabla\rho$ will typically produce a poor approximation ($||\nabla p - \nabla p_h||_{\mathrm{L}_2} = \mathcal{O}(1)$ at best) and is unlikely to converge (Heister *et al.* 2017). Hydrostatic pressure, defined as $\nabla p_s = \rho^*\boldsymbol{g}$ following an adiabatic reference density, dominates the Earth's mantle. Therefore, $\nabla\rho(p, T) \approx \frac{\partial\rho}{\partial p}\ \rho^*\boldsymbol{g} + \frac{\partial\rho}{\partial T}\ \nabla T$. The weak form of the continuity equation multiplied by the test function q is

$$-\left(\nabla\cdot\boldsymbol{u}, q\right) + \left(\frac{\nabla\rho^*}{\rho^*}\cdot\boldsymbol{u}, q\right) = 0, \tag{9}$$

where $\frac{\nabla\rho^*}{\rho^*} = (\frac{\partial\rho}{\partial p}\boldsymbol{g} + \frac{1}{\rho^*}\frac{\partial\rho}{\partial T}\nabla T^*)$.

All methods of approximation introduce various errors. Here, errors will depend on how accurately $\rho^* = \rho(p^*, T^*)$, where p^* and $T*$ follow an adiabatic profile, approximates $\rho = \rho(p, T)$. Boundary conditions are imposed using a combination of prescribed stress and velocity, namely:

$$\boldsymbol{u} = \boldsymbol{u}_{\text{prescribed}} \qquad \text{on } \Gamma_{\text{prescribed},\ \boldsymbol{u}} \tag{10}$$

$$2\eta\left(\epsilon\left(\boldsymbol{u}\right) - p\boldsymbol{I}\right)\boldsymbol{n} = \boldsymbol{d} \qquad \text{on } \Gamma_{\text{traction},\ \boldsymbol{u}} \tag{11}$$

where $\Gamma_{\text{prescribed},\ \boldsymbol{u}}$ is the boundary over which the flow velocity is prescribed and $\Gamma_{\text{traction},\ \boldsymbol{u}}$ is the boundary on which traction is prescribed to a chosen surface force density $\boldsymbol{d}$ (including zero).

The weak forms of the momentum and mass equations (eqs 6 and 9, respectively) in combination with selected boundary conditions (eqs 10 and 11) form the general matrix equation for the discrete Stokes problem:

$$\begin{pmatrix} \boldsymbol{A} & \boldsymbol{B}^T \\ \boldsymbol{B}+\boldsymbol{C} & 0 \end{pmatrix}\begin{pmatrix} \hat{\boldsymbol{u}} \\ \hat{\boldsymbol{p}} \end{pmatrix} = \begin{pmatrix} \hat{\boldsymbol{f}} \\ 0 \end{pmatrix}, \tag{12}$$

where $\hat{\boldsymbol{u}}$, $\hat{\boldsymbol{p}}$ and $\hat{\boldsymbol{f}}$ are the velocity, pressure and force ($\boldsymbol{f} = \rho\boldsymbol{g}$) vectors, respectively. $\boldsymbol{A}$ is the stiffness matrix, $\boldsymbol{B}^T$ is the discrete divergence operator, $\boldsymbol{B}$ is the discrete gradient operator and $\boldsymbol{C}$ comes from the second term in eq. (9). Matrices $\boldsymbol{A}$, $\boldsymbol{B}$ and $\boldsymbol{C}$ are constructed using shape functions $\{\emptyset_i\}_i$, which satisfy the prescribed boundary conditions (eqs 10 and 11). The nonlinearity within the linearized mass conservation equation is iterated out using a nonlinear solver. Further, the non-symmetric matrix (eq. 12) constructed with compressible flow will require more costly linear solvers than a symmetric matrix corresponding to incompressible flow.

2.1.2 Consistent boundary flux method

The CBF method occurs during post-processing since the solutions to the governing equations of the Stokes system (eq. 12) remain unchanged. Below we outline the equations necessary for the CBF method modified from the procedure described in Burstedde *et al.* (2013). We assume a free-slip boundary condition on $\partial\Omega$ has been imposed to form matrix eq. (12), specifically,

$$\boldsymbol{u}\cdot\boldsymbol{n} = 0, \quad \boldsymbol{v}\cdot\boldsymbol{n} = 0, \tag{13}$$

$$\boldsymbol{t}\cdot\left[\left(2\eta\left(\epsilon\left(\boldsymbol{u}\right) - \frac{1}{3}\left(\nabla\cdot\boldsymbol{u}\right)\boldsymbol{I}\right) - p\boldsymbol{I}\right)\boldsymbol{n}\right] = 0, \tag{14}$$

where $\boldsymbol{t}$ is any tangential vector. Recall that the boundary integral was removed when integration by parts was performed on the momentum eq. (5). The boundary term, which we represent with D, contains the boundary integral required to compute the normal component of the traction vector. The boundary term (multiplied by test function $\boldsymbol{v}$) from eq. (5) in integral form reads

$$D\left(p, \boldsymbol{u}, v\right) = \int_{\partial\Omega}\left[\left(2\eta\left(\epsilon\left(\boldsymbol{u}\right) - \frac{1}{3}\left(\nabla\cdot\boldsymbol{u}\right)\boldsymbol{I}\right) - p\boldsymbol{I}\right)\boldsymbol{n}\right]\cdot\boldsymbol{v}. \tag{15}$$

Assuming a solution $(\boldsymbol{u}, p)$ exists that satisfies boundary conditions (13) and (14), eq. (15) can be rewritten as

$$D\left(p, \boldsymbol{u}, v\right) = \int_{\partial\Omega}\left(\boldsymbol{v}\cdot\boldsymbol{n}\right)s, \tag{16}$$

where $s = \boldsymbol{n}\cdot[(2\eta(\epsilon(\boldsymbol{u}) - \frac{1}{3}(\nabla\cdot\boldsymbol{u})\boldsymbol{I}) - p\boldsymbol{I})\boldsymbol{n}]$ is the normal component of the traction vector. A discretized normal vector field on the boundary is constructed as

$$\boldsymbol{v}\left(\boldsymbol{x}\right) = \sum_{i|x_n\in\partial\Omega} v_i\boldsymbol{n}_i\emptyset_i\left(\boldsymbol{x}\right). \tag{17}$$

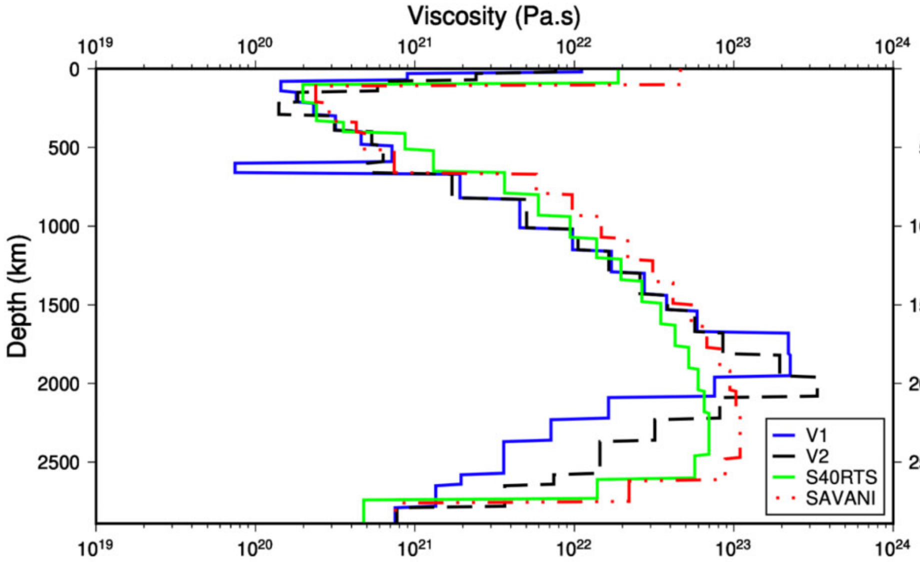

Figure 1. Four radial viscosity profiles adopted in our dynamic topography models. V1 and V2 are taken from Mitrovica & Forte (2004) and Forte *et al.* (2010). S40RTS and SAVANI are taken from Steinberger (2016).

Eq. (17) is defined by a coefficient vector $\bar{\boldsymbol{v}} = \{v_i\}_i$, where index i loops over the shape functions $\emptyset_i$ on the boundary. Vector $\bar{\boldsymbol{n}} = \{\boldsymbol{n}_i\}_i$ contains the normal values for all boundary nodes x_i. By inserting eq. (17) into the weak form of the momentum equation and arranging the terms corresponding to the coefficient vector, a system of equations is constructed for the discretized normal traction $s = \Sigma_i s_i \emptyset_i$ with nodal values $\bar{\boldsymbol{s}} = \{\boldsymbol{s}_i\}_i$:

$$\bar{\boldsymbol{M}}\bar{\boldsymbol{s}} = \left(\bar{\boldsymbol{f}} - \bar{\boldsymbol{A}}\hat{\boldsymbol{u}} - \bar{\boldsymbol{B}}^T\hat{\boldsymbol{p}}\right) \cdot \boldsymbol{n}. \tag{18}$$

The surface mass matrix,

$$\bar{\boldsymbol{M}}_{ij} = \int_{\partial\Omega} \emptyset_i(\boldsymbol{x})\, \emptyset_j(\boldsymbol{x})\, \mathrm{d}x, \tag{19}$$

is derived from the boundary integral in eq. (14), with indices i, j limited to boundary nodes. Therefore, eq. (18) computes the normal vectors only at boundary nodes.

The normal vectors at boundary nodes can now be incorporated when determining radial stress,

$$\sigma_{rr} = 2\eta\left(\epsilon(\boldsymbol{u}) - \frac{1}{3}(\nabla\cdot\boldsymbol{u})\,\boldsymbol{I}\right) - p\boldsymbol{I}, \tag{20}$$

which was computed using only volume integrals prior to the implementation of the CBF method. Radial stress is required to compute dynamic topography,

$$h = \frac{\sigma_{rr}}{(\boldsymbol{g}\cdot\boldsymbol{n})\,\rho}, \tag{21}$$

where ρ is the difference in density between the mantle and the overlying (deforming) material and $\boldsymbol{g}$ is gravitational acceleration.

Both the current version of ASPECT and versions of ASPECT prior to the release of version 2.0.0 use eqs (20) and (21) to compute dynamic topography. However, the CBF method computes eq. (20) with higher accuracy because it incorporates boundary integrals (which was removed in eq. 5 and recovered in eqs 16–19), allowing the normal stress to be computed on surface boundary nodes consistent with the solution to a Stokes system with prescribed boundary conditions. Without the CBF method, eq. (20) is computed using volume integrals only. Zhong *et al.* (1993) show that the CBF algorithm increases accuracy by about one order of magnitude over the standard pressure smoothing method. The CBF method is also validated by the benchmark study reported in Liu & King (2019). Using the CBF method in ASPECT for 3-D spherical incompressible flow, Liu and King computed response functions of dynamic topography, horizontal velocity and geoid kernels at the surface and core–mantle boundary to compare with semi-analytical solutions determined by the propagator matrix method from Hager & O'Connell (1981). The numerical results with the model set-up most aligned with this study (without self-gravitation and assuming a layered viscosity) were in excellent agreement with the semi-analytical solution for dynamic topography with relative differences generally within 1 per cent demonstrating the efficacy of the CBF method.

2.2 Model parametrizations

We calculate dynamic topography on a spherical shell using eight different model set-ups that vary the temperature perturbations in the mantle, the viscosity and the boundary condition imposed. Our approach is similar to that of Austermann *et al.* (2017). Pressure, density and gravity are depth-dependent and radially symmetric (Supporting Information Fig. S1), and we test four radially symmetric viscosity models (Fig. 1). Four tests are based on the density model TX2008 (Simmons *et al.* 2009). TX2008 is based on a joint inversion of shear wave traveltime data and convection-related constraints (free-air gravity, core–mantle boundary excess ellipticity, tectonic plate motions and dynamic surface topography) for a radially symmetric relationship between shear wave speed and density (Simmons *et al.* 2009). Two tests use the shear wave tomography model S40RTS, which is a shear wave velocity model (up to degree 40) for Earth's whole mantle that is based on a collection of Rayleigh wave phase velocities for the upper third of the mantle, teleseismic body-wave traveltimes for the lower two thirds of the mantle and normal mode-splitting functions for whole mantle constraints, particularly at the longest wavelengths (Ritsema *et al.* 2011). The final two tests use the shear wave tomography model SAVANI, which is a radially anisotropic shear wave velocity model that is based on a compilation of surface wave phase delays and cross-correlation traveltimes of major body

Table 1. Physical parameters and values employed in simulations.

Parameter	Value	Unit
Outer shell radius[a]	6371	km
Inner shell radius[a]	3481	km
Adiabatic surface temperature[a]	1600	K
Outer shell temperature[a]	1600	*K*
Inner shell temperature[a]	2440	*K*
Reference density[a]	3300	$\mathrm{kg\,m^{-3}}$
Reference compressibility[b]	4×10^{-12}	$\mathrm{Pa^{-1}}$
Heat capacity[c]	1.25×10^{3}	$\mathrm{J\,kg^{-1}\,K^{-1}}$
Thermal expansion (outer shell)[c]	3.5×10^{-5}	$\mathrm{K^{-1}}$
Thermal expansion (670 km)[c]	2.5×10^{-5}	$\mathrm{K^{-1}}$
Thermal expansion (inner shell)[c]	1.0×10^{-5}	$\mathrm{K^{-1}}$

[a] Austermann *et al.* (2017).
[b] Bangerth *et al.* (2020).
[c] Glisovic & Forte (2015).

wave phases and variable block parametrization adapted to local ray path density (Auer *et al.* 2014). For our tests using S40RTS and SAVANI, density perturbations were calculated following the depth-dependent seismic velocity to density conversion profile by Steinberger (2016).

We pair the TX2008 density models with two radial viscosity profiles, V1 and V2 (Fig. 1), originally from Mitrovica & Forte (2004) then refined in Forte *et al.* (2010). V1 and V2 were derived from joint inversions of convection-related observables including free-air gravity harmonics, core-mantle boundary ellipticity and tectonic plate motions combined with glacial isostatic adjustment data related to the melting of the Laurentide and Fennoscandian ice sheets (Forte *et al.* 2010). Viscosity profiles V1 and V2 are largely similar in the upper mantle, the main difference being a low viscosity 'notch' in the transition zone in V1, which uncouples upper- and lower-mantle flows. Viscosity profile V2 has a higher deep-mantle viscosity (by a factor of ∼5). For shear wave tomography models S40RTS and SAVANI, a depth-dependent viscosity profile is chosen specific to each tomography model from Steinberger (2016, fig. 1). Both profiles are derived based on mineral physics and optimized to fit heat flux, geoid, normalized gravity and present-day dynamic topography.

Our models assume compressible flow, therefore temperature and density follow an adiabatic reference profile. We impose an adiabatic surface temperature of 1600 K, which sets the starting point for nonlinear solvers to compute adiabatic conditions for the temperature field throughout the mantle. Therefore, we do not impose a thermal boundary layer, however our models do include temperature perturbations associated with the oceanic lithosphere. Depth-dependent heat capacity, thermal conductivity and thermal expansivity are adopted from Glisovic & Forte (2015, table 1). For all eight tests, reference surface density is set to 3300 kg $\mathrm{m^{-3}}$. Depth and buoyancy variations of the continental lithosphere in the SAVANI and S40RTS-based models are parametrized using the formulation from Steinberger (2016). This set-up is consistent with the Austermann *et al.* (2017) approach (Table 1).

A radial gravity profile is imposed from Glisovic & Forte (2015), where the gravity field was obtained by integrating a depth-dependent density profile taken from the Earth model PREM (Dziewonski & Anderson 1981). A free-slip boundary condition is applied at the core-mantle boundary. We test all four Earth models (TX2008-V1, TX2008-V2, S40RTS and SAVANI) with the top surface boundary conditions no-slip and free-slip. We use a variable refinement such that in the upper 1000 km, the depth resolution of the grid is ∼30 km and the lateral resolution is ∼80 km (refinement 5). Below 1000 km, the resolution ranges from 65 to 115 km with depth and 175 to 250 km laterally (refinement 3).

A flexible generalized minimal residual (GMRES) iterative scheme is used to solve the linear compressible Stokes system. The linear solver tolerance is set to the lowest value that allows convergence, which ranges from 10^{-5} to 10^{-3} depending on the model set-up. The non-linear solver tolerance is set to 10^{-5}. Linear elements are used for pressure and quadratic elements are used for velocity satisfying the LBB (Ladyzhenskay–Babuska–Brezzi) stabilization condition (Brezzi & Douglas 1988).

The convection simulations are run forward in time for 3 million years. We use a bicubic spline interpolation to estimate dynamic topography at every 0.1° latitude and longitude. The average rate of change since 3 Ma is computed by subtracting instantaneous dynamic topography estimates at present-day from estimates at 3 Ma and dividing that result by 3 Myr. The rate of change is for points fixed in space, rather than moving tectonic plates. We calculate the average of all 8 experiments for our final instantaneous present-day and rate of change of dynamic topography solutions. Our code, parameter files, input files and model output files are made available on Zenodo (Williams *et al.* 2023) for reproducibility. We test the eight model set-ups with and without the CBF method.

3 RESULTS AND DISCUSSION

Here, we present the total average (across all eight models) instantaneous present-day and rate of change of dynamic topography solutions computed with the CBF method, without the CBF and the residuals. We then discuss some of the geophysical implications of dynamic topography results (with and without CBF) for the US East Coast. Between the two approaches, we observe a trend of spatial similarities with generally higher magnitudes in estimates in dynamic topography calculations with the CBF algorithm implemented. Our average (across all eight models) present-day instantaneous estimates with the CBF method have minimum and maximum values of −1466 and 2103 m, respectively, while our average estimates of dynamic topography without the CBF method range from −1266 to 1861 m. We observe the highest instantaneous present-day amplitudes in the Afar Region labelled A in Fig. 2(a) (2103 m with the CBF and 1861 without the CBF) and at the divergence of the Pacific Plate and the Nazca Plate labelled B in Fig. 2(a) (2079 m with CBF and 1785 without CBF). We observe the lowest dynamic topography magnitudes in Iran near the Persian Gulf labelled C in Fig. 2(a) (−1466 m with CBF and −1241 m without CBF) and near the border of Bhutan and Bangladesh labelled D in Fig. 2(a) (−1452 m with CBF and −1266 without CBF). The highest amplitudes for the rate of change of dynamic topography since 3 Ma occur at the eastern coast of Mexico labelled A in Fig. 2(a) (0.093 mm $\mathrm{yr^{-1}}$ with the CBF and 0.077 mm $\mathrm{yr^{-1}}$ without the CBF) and central Saudi Arabia labelled B in Fig. 2(a) (0.089 mm $\mathrm{yr^{-1}}$ with the CBF and 0.074 mm $\mathrm{yr^{-1}}$ without the CBF). The lowest magnitudes of rate of change of dynamic topography since 3 Ma occur on the boundary between the Pacific Plate and the Cocos Plate labelled C in Fig. 2(a) (−0.072 mm $\mathrm{yr^{-1}}$ with the CBF and −0.056 mm $\mathrm{yr^{-1}}$ without the CBF) and the Afar region labelled D in Fig. 2(d) (–0.067 mm $\mathrm{yr^{-1}}$ with the CBF and −0.053 mm $\mathrm{yr^{-1}}$ without the CBF). While these values demonstrate the differences in magnitudes with and without the CBF, we note that these models are likely least reliable at active margins because it does not capture crustal deformation processes.

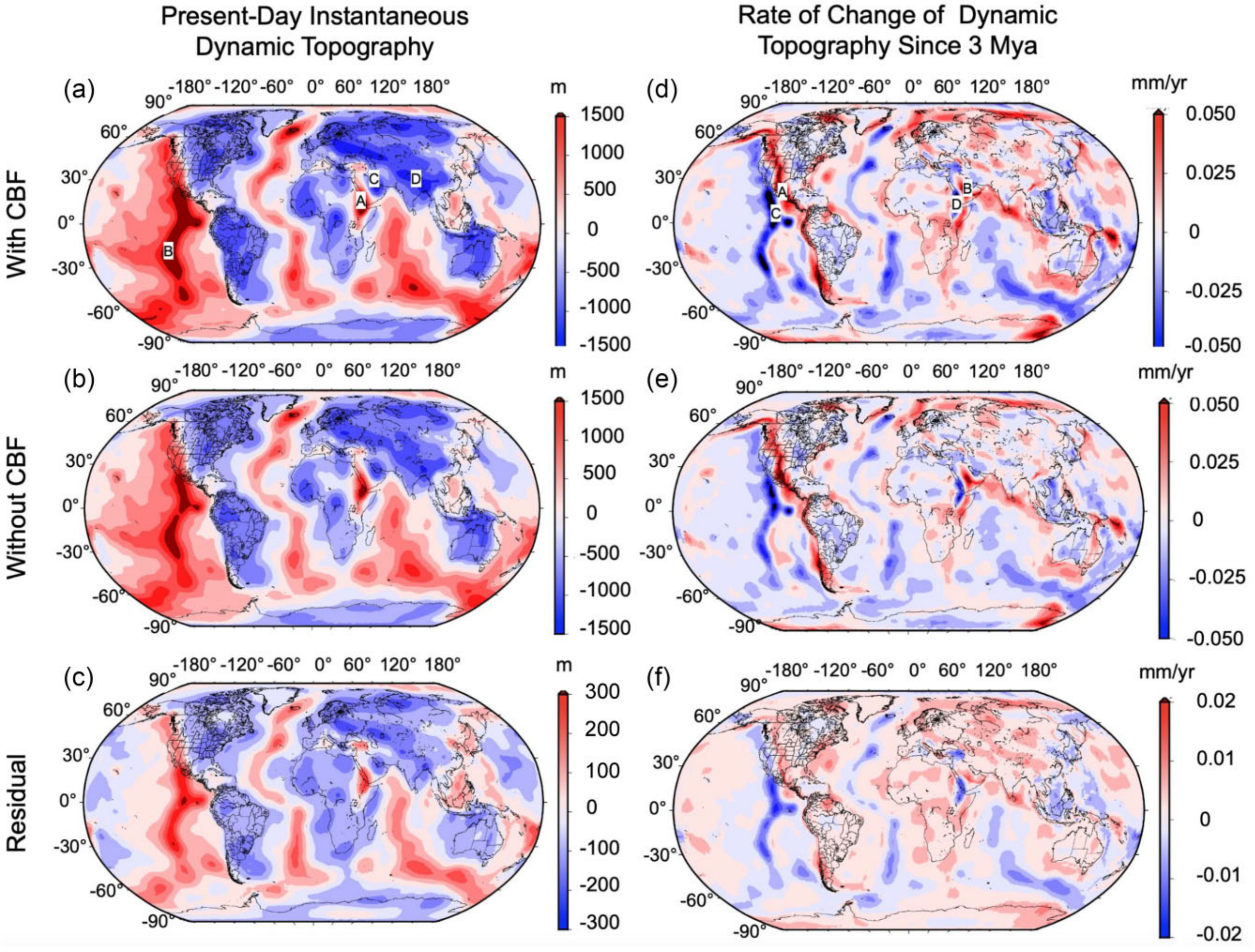

Figure 2. Global average (over all eight model set-ups) present-day instantaneous dynamic topography (with and without CBF), rate of change of dynamic topography since 3 Ma (with and without CBF) and the residuals (CBF − no CBF).

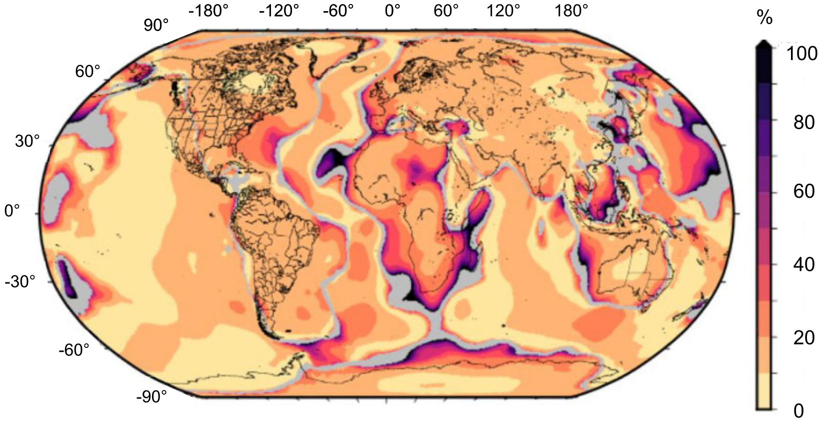

Figure 3. Average absolute value of per cent changes between present-day instantaneous dynamic topography estimates with and without the CBF method averaged over all models. Grey areas are regions that are excluded in the per cent change calculation.

Fig. 3 shows the average absolute value of per cent changes for instantaneous present-day dynamic topography over all eight models with and without CBF relative to no CBF. Regions in which dynamic topography (with and without CBF) are between −100 and +100 m are excluded and coloured as grey since relatively small dynamic topography differences in these regions lead to high, unrepresentative percentage changes. The highest per cent changes occur throughout the African continent and surroundings, particularly along the eastern coast. The region where the second highest per cent changes occur is in the Pacific Ocean east of Asia through the Philippines and Indonesia. The lowest per cent changes occur elsewhere in the Pacific Ocean and the Indian Ocean. The total

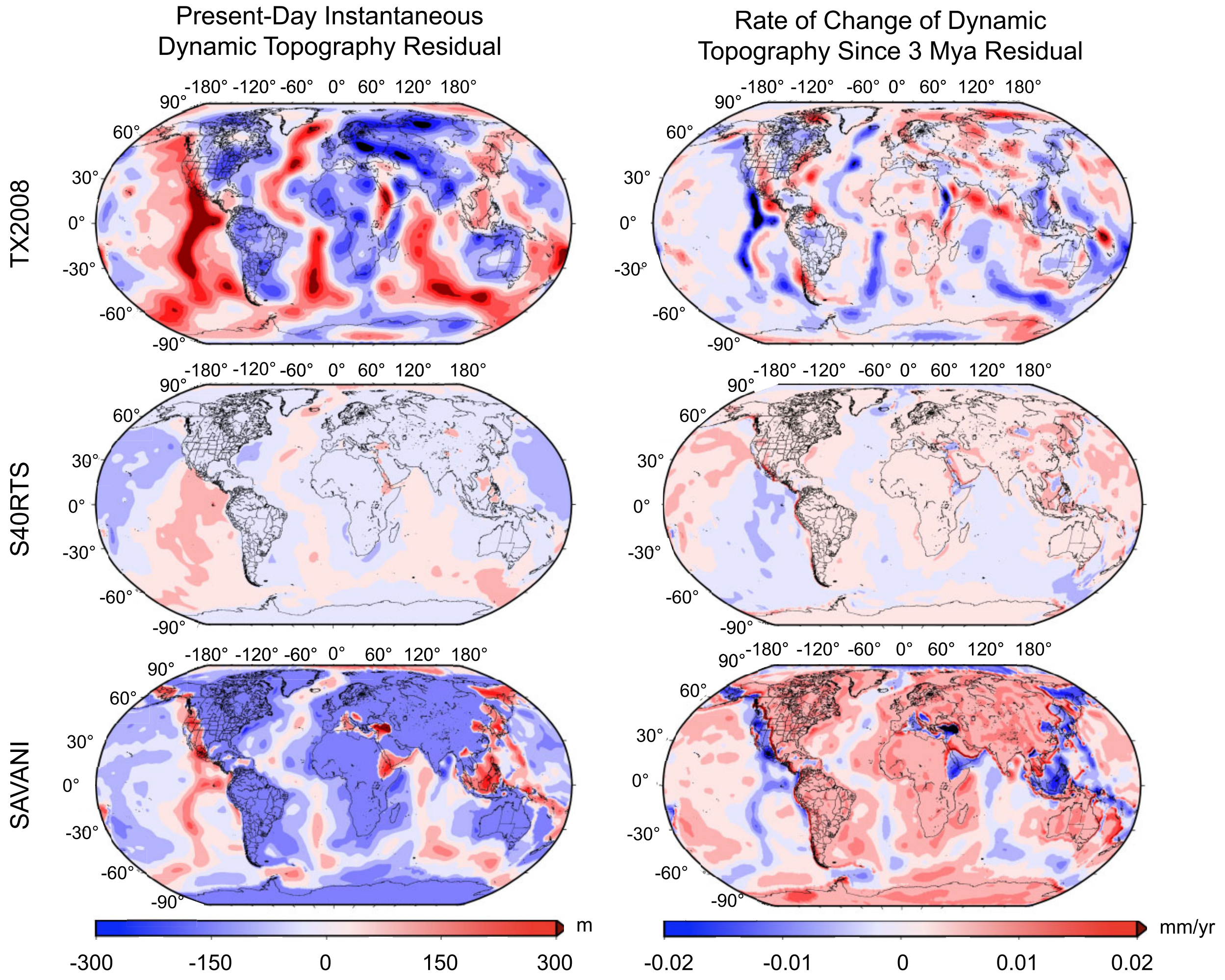

Figure 4. Residuals of global present-day instantaneous dynamic topography and rate of change of dynamic topography since 3 Ma constrained by temperature model (average over both boundary conditions). Top: TX2008 (average over both viscosity profiles). Middle: S40RTS. Bottom: SAVANI.

average for the absolute value of per cent changes globally is approximately 15 per cent with a standard deviation of approximately 11 per cent.

To assess the influence of the CBF method when using different temperature models, we calculate the average present-day instantaneous global dynamic topography and the average rate of change of global dynamic topography since 3 Ma with and without the CBF method isolated by temperature models TX2008 (includes both viscosity profiles and boundary conditions), S40RTS (includes both boundary conditions) and SAVANI (includes both boundary conditions). Fig. 4 shows the residuals of present-day instantaneous dynamic topography and rate of change of dynamic topography since 3 Ma for each temperature model. While the topographies and residuals are strongly correlated for TX2008, we observe a relatively constant magnitude change over the continents with S40RTS and SAVANI. Computing radial stress directly at surface boundary nodes (CBF method) accounts for the differences in residual shapes between TX2008, S40RTS and SAVANI because with CBF, the density anomalies are accounted for all the way to the surface of the model. While TX2008 is a density model, S40RTS and SAVANI use a prescribed constant density over continents following Steinberger (2016), which overrides the density that would be calculated from seismic velocities. Further, the continental lithosphere density anomaly for SAVANI and S40RTS is 0.5 and 0.1 per cent, respectively, which explains the larger residuals for SAVANI. We acknowledge that our model set-ups contain certain simplifications (e.g. radial viscosity and no thermal boundary layer) that will affect our results.

We find that TX2008 has the highest residuals with an average per cent change for instantaneous dynamic topography of 23 per cent; SAVANI has a 17 per cent change, and S40RTS has a 9 per cent change. See Supporting Information Figs S2 snd S3 for the present-day instantaneous and the rate of change since 3 Ma of dynamic topography, respectively, with and without the CBF method for each temperature model. Further, we explore the global average present-day instantaneous (Supporting Information Fig. S4) and the global average rate of change of dynamic topography since 3 Ma (Supporting Information Fig. S5) isolated by boundary conditions no-slip and free-slip. The no-slip boundary condition produces higher residuals with an 18 per cent change than a free-slip boundary condition, which has a 12 per cent change.

3.1 Geophysical implications of the East Coast of the United States

The East Coast of the United States is considered a passive margin associated with the break-up of Pangaea at ∼180 Ma. Unlike

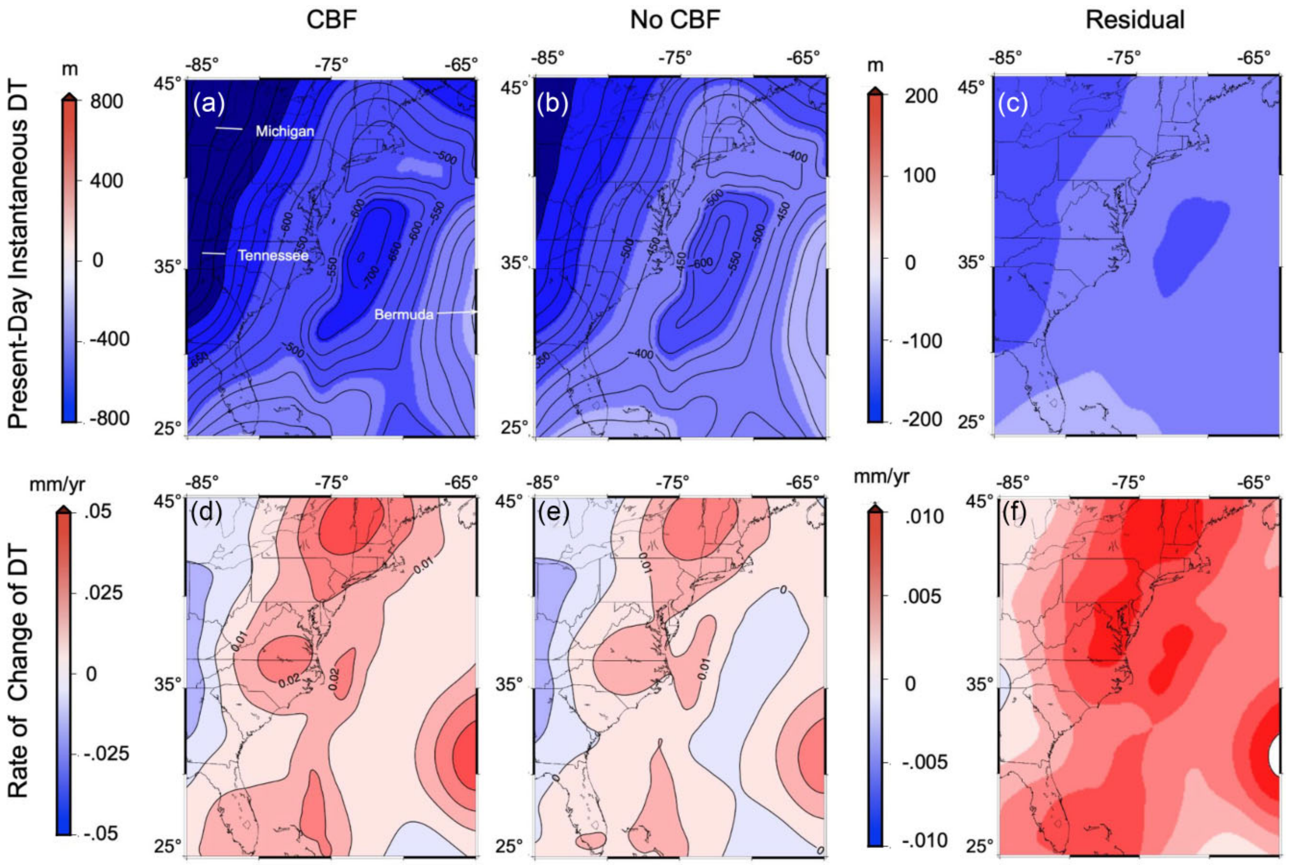

Figure 5. Present-day instantaneous dynamic topography (with and without CBF) averaged over all models, rate of change of dynamic topography since 3 Ma (with and without CBF) averaged over all models and the residuals (CBF—No CBF) on the US East Coast.

most seismically quiet passive margins, occasional shallow, low magnitude seismicity occurs along the East Coast (Stover & Coffman 1992), although there is no active volcanism. The approximately 100-million-year-old Farallon slab currently lies beneath the East Coast of the United States, which has been imaged with seismic tomography between 1300-1750 km depths (i.e. Schmid *et al.* 2002; Lu *et al.* 2019). It has been proposed that the cold, dense slab is inducing mantle downwelling, promoting negative dynamic topography (i.e. Bertelloni & Gurnis 1997). While Spasojevic *et al.* (2009) support this argument for dynamic subsidence on the US East Coast, Rowley *et al.* (2013) conclude that the existence of hot, buoyant material in the shallow mantle (hypothesized to be asthenospheric return flow) is key in shaping partially uplifting patterns of dynamic topography along the East Coast.

Fig. 5 shows the average (across all eight models) instantaneous present-day dynamic topography and rate of change of dynamic topography since 3 Ma with and without the CBF, and the residuals on the East Coast of the United States. Amplitudes for instantaneous present-day dynamic topography and rate of change of dynamic topography since 3 Ma calculated with the CBF are −294 m at 65°W, 32.6°N near Bermuda (located approximately a quarter of a longitude off the map in Fig. 5a) and 0.037 mm yr^{-1} at 65°W, 31.1°N near Bermuda. Minimum values are −1007 m at 85°W, 43.1°N in central Michigan and −0.019 mm yr^{-1} at 85°W, 35.2°N in eastern Tennessee. Amplitudes for instantaneous present-day dynamic topography and rate of change of dynamic topography since 3 Ma calculated without the CBF are −212 m at 65°W, 32.6°N near Bermuda and 0.026 mm yr^{-1} at 65°W, 31.1°N near Bermuda. Minimum values are −850 m at 85°W, 42.7°N in central Michigan and −0.018 mm yr^{-1} at 85°W, 35.1°N in eastern Tennessee. The average absolute value of per cent changes for instantaneous present-day dynamic topography for the plotted region is approximately 25 per cent. We also explore the average present-day instantaneous dynamic topography and rate of change of dynamic topography since 3 Ma with and without the CBF method on the US East Coast isolated by the average temperature models TX2008, S40RTS and SAVANI (over both boundary conditions; see Supporting Information Figs S6 and S7) and the average boundary conditions no-slip and free-slip (over all three temperature models; see Supporting Information Figs S8 and S9).

Pliocene shoreline reconstructions have been used to understand the interplay between dynamic topography, glacial isostatic adjustment, sediment loading, thermal subsidence and flexural loading on the US East Coast. The Orangeburg scarp (Fig. 6a) has been used as a mid-Pliocene sea level marker in numerous studies (i.e. Rowley *et al.* 2013; Rovere *et al.* 2015; Moucha & Ruetenik 2017) to understand the contribution from these different processes to past vertical land motions and sea level heights. Rowley *et al.* (2013) modelled dynamic topography since 3 Ma and concluded that dynamic topography and, to a lesser extent, glacial isostatic adjustment account for the warped surface of the Orangeburg scarp. Rowley *et al.* (2013) tested four different model set-ups, and although their preferred model fits the trend of the Pliocene shoreline relatively well, they recognized that large uncertainties exist in these dynamic topography estimates and vary significantly depending on the viscosity and buoyancy structure of the mantle. Further, contributions from flexural isostasy due to sediment loading and erosional unloading were not considered in Rowley *et al.* (2013). Rovere *et al.*

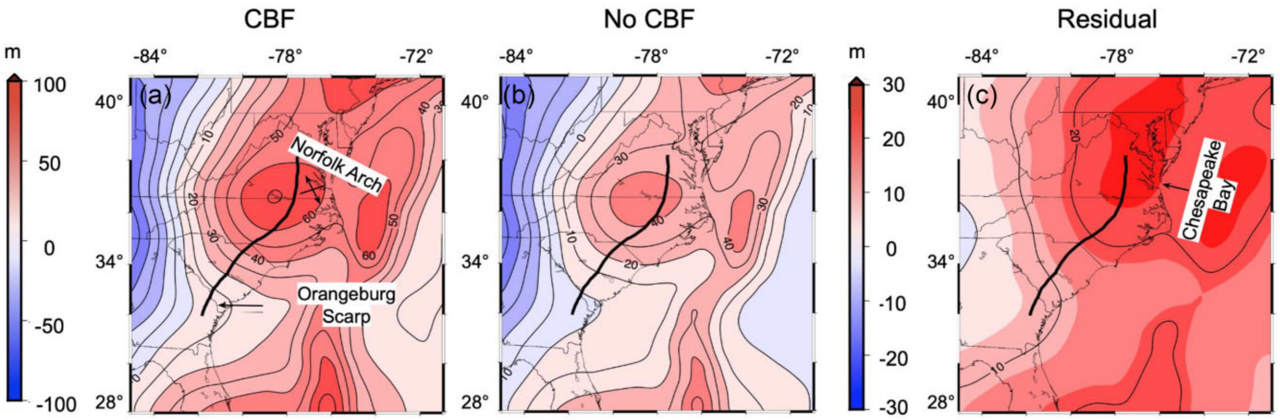

Figure 6. Average (over all eight models) change in dynamic topography over the past 3 million years with the CBF (left), without the CBF (middle) and the residual (right).

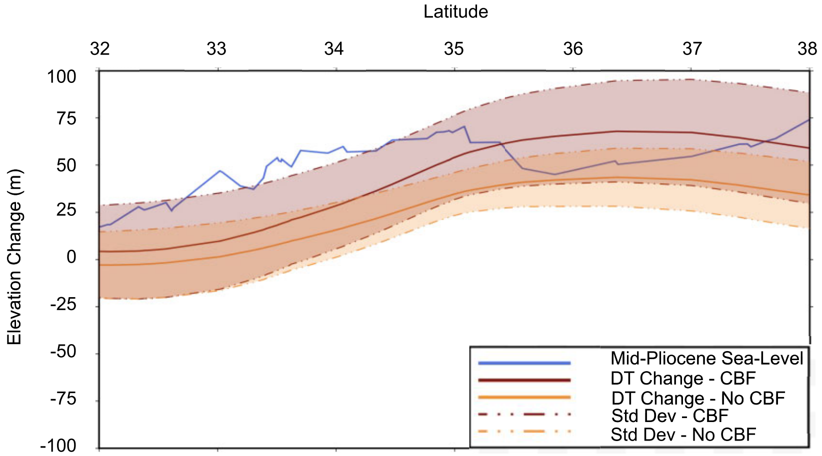

Figure 7. Average (over all eight models) elevation change due to change in dynamic topography with and without CBF over the past 3 million years by increasing latitude along the Orangeburg scarp. The shaded regions show the standard deviation between the eight different model set-ups. The blue line shows the elevation changes of the mid-Pliocene shoreline accounting for GIA and assuming a 14 m eustatic sea level difference between the mid-Pliocene and present-day from Rovere *et al.* (2015).

(2015) accurately remapped the Orangeburg scarp and corrected the shoreline elevation for glacial isostatic adjustment to compare with the dynamic topography estimates using the four model set-ups from Rowley *et al.* (2013). Though Rovere *et al.* (2015) found fits to the general trends in the mid-Pliocene shoreline elevations, they noted that many local discrepancies still exist. Moucha & Ruetenik (2017) then produced a landscape evolution model demonstrating that flexural isostasy is needed to explain the warping along the Orangeburg scarp based on the mid-Pliocene shoreline elevation constructed in Rovere *et al.* (2015).

We investigate how dynamic topography predictions with and without CBF can affect the interpretation of the Orangeburg scarp (Fig. 6). The Orangeburg scarp lies along the US Atlantic Coast from Georgia to Virginia and was formed as the mid-Pliocene (∼3 Ma) shoreline (Rowley *et al.* 2013). The Orangeburg scarp, which would have been horizontal at the time of formation, shows up to 60 m of variations in elevation (Rowley *et al.* 2013). This warping is thought to reflect post mid-Pliocene elevation changes due to dynamic topography, glacial isostatic adjustment and contributions from flexural isostasy due to sediment loading and erosional unloading (Rowley *et al.* 2013; Rovere *et al.* 2015; Moucha & Ruetenik 2017). Fig. 6 shows our computed change in dynamic topography over the past 3 million years with CBF, without CBF and the residual. The range of dynamic topography change with the CBF method is −56 to 75 m, while the range without the CBF method is −54 to 52 m. The pattern along the Orangeburg scarp is largely similar between the two approaches with an increasing change in dynamic topography moving northwards and a peak change near the Chesapeake Bay (labelled in Fig. 6c) by the Norfolk Arch (labelled in Fig. 6a). However, we observe a significantly higher change in dynamic topography with the CBF method. The cumulative change in dynamic topography over the past 3 million years at the peak (near the Norfolk Arch) with and without CBF is 69 m and 47 m, respectively.

On the US East Coast, differences in estimates of dynamic topography changes can significantly alter interpretations drawn from the mid-Pliocene shoreline preserved in the Orangeburg scarp. Fig. 7 shows change in dynamic topography since 3 Ma from south to north along the Orangeburg scarp with and without the CBF method. The shaded regions show the standard deviations of dynamic topography changes (with and without CBF) between our 8 different model set-ups. As a reference, we include the elevation changes of the mid-Pliocene shoreline accounting for GIA and assuming a 14 m eustatic sea level difference between the mid-Pliocene and present-day from Rovere *et al.* (2015). Our peak elevation change at 36.4°N with and without the CBF is approximately 68 and

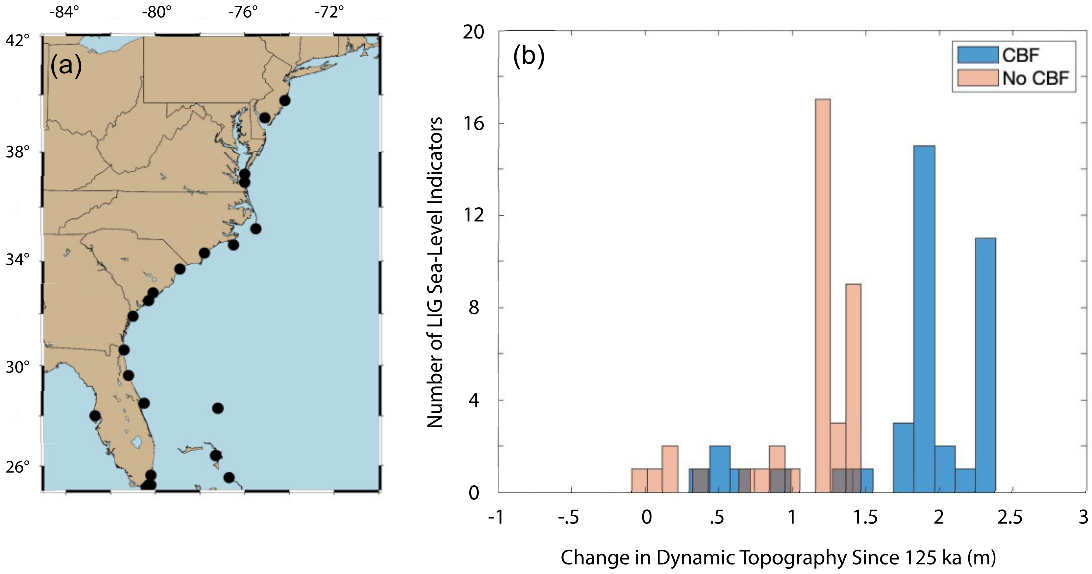

Figure 8. (a) Locations of sea level indicators included in the distribution in 8B. (b) Distribution of change in dynamic topography over the past 125 k years with and without CBF at sea level markers from the LIG sea level marker compilation from Austermann *et al.* (2017).

43 m, respectively. This 25 m difference in elevation change can lead to vastly different interpretations of the mid-Pliocene shoreline. It is important to note that standard deviations across the eight models are nearly as high as the computed average change in dynamic topography. See Supporting Information Fig. S10 for the change in dynamic topography over the past 3 My along the Orangeburg scarp for each model set-up. Further, we do not account for plate motion (Hoggard *et al.* 2021), therefore these values of dynamic topography change cannot be directly compared to shoreline elevations. We are simply using the Orangeburg scarp as a case study to demonstrate how the CBF method can significantly alter geophysical and geomorphological implications. A greater change in dynamic topography would lead to different interpretations of the mid-Pliocene shoreline and past sea level changes. This would also suggest that a smaller contribution to the warping of the Orangeburg scarp from isostatic processes such as glacial isostatic adjustment and flexural isostasy from sediment transport is required to explain the present elevation of the scarp.

Austermann *et al.* (2017) computed vertical deflections due to dynamic topography to compare with a global set of LIG sea level markers. They found that predictions of changes in dynamic topography since 125 ka were correlated with patterns in LIG sea level marker elevations, but the magnitudes of predicted changes were overall lower than observed changes. We evaluate the distribution of changes in dynamic topography on the US East Coast over the past 125 ka years with and without CBF at LIG sea level marker locations using the compilation from Austerman *et al.* 2017 (Fig. 8). The mean dynamic topography changes over the past 125 ka years with and without CBF are 1.84 and 1.07 m, respectively. This result suggests that one possible reason for the misfit between the magnitudes of dynamic topography changes and observed sea level changes in Austermann *et al.* (2017) is a result of dynamic topography being computed using ASPECT prior to the implementation of the CBF method. The global mean dynamic topography changes over the past 125 k years with and without CBF for all sea level markers from Austermann *et al.* (2017) is 1.38 and 1.08 m, respectively. See Supporting Information Fig. S11 for the distribution of dynamic topography changes over the past 125 ka years with and without CBF for all global sea level markers. Austermann *et al.* (2017) notes that 2 m of global mean sea level rise equates to over half the ice volume expected in melting of the West Antarctic Ice Sheet. Therefore, even slight improvements in the accuracy of estimates for dynamic topography would improve Pleistocene sea level reconstructions, which can help to better understand past sea level changes and ice sheet stability.

4 CONCLUSIONS

In this study we investigate the effects of the CBF post-processing method on dynamic topography estimates using ASPECT. Uncertainties in previously published dynamic topography estimates remain significant due to poorly constrained properties in Earth's compositional structure. The CBF method, which is used to calculate radial stresses at the surface, was recently implemented in ASPECT. It has been shown that the CBF algorithm improves the accuracy of dynamic topography calculations by approximately one order of magnitude. We use the tomography models TX2008, S40RTS and SAVANI, each tested with a corresponding radial viscosity profile (2 for TX2008), and two different boundary conditions for a total of eight experiments. We run the simulations with and without the CBF method, which takes place during post-processing and does not affect the velocity solution solved by the Stokes system. Our dynamic topography calculations show similar spatial consistency in both approaches, but generally indicate an increase in magnitude for both present-day instantaneous dynamic topography and rate of change of dynamic topography since 3 Ma using the CBF method. The average per cent change for present-day instantaneous dynamic topography between the two approaches is approximately 14 per cent and the per cent change for rate of change of dynamic topography since 3 Ma is approximately 76 per cent; therefore, we conclude that the implementation of the CBF algorithm significantly influences dynamic topography calculations in ASPECT. We explore the geophysical implications of improved estimates of dynamic topography on the East Coast of the United States using the interpretation of the Orangeburg scarp as a case study. A greater change in dynamic topography would significantly alter interpretations of the mid-Pliocene shoreline and, therefore, past sea level changes and ice sheet stability, and may suggest a smaller contribution to the warping of the Orangeburg scarp from glacial isostatic adjustment and flexural isostasy due to sediment transport. Overall, enhanced accuracy in dynamic topography calculations can be used to better evaluate the effects on surface processes including vertical motions, sea level change and sedimentation and erosion. Further, relevant publications that calculated dynamic topography without the CBF algorithm, independent of the specific software package used, may need to be readdressed.

ACKNOWLEDGMENTS

We thank the Computational Infrastructure for Geodynamics (geodynamics.org) which is funded by the National Science Foundation under award EAR-0949446 and EAR-1550901 for supporting the development of ASPECT. We thank Bernard Steinberger and an anonymous reviewer for constructive reviews that improved this manuscript.

Funding: This material is based upon work supported by the U.S. Geological Survey under Grant/Cooperative Agreement No. G21AC10016. The views and conclusions contained in this document are those of the authors and should not be interpreted as representing the opinions or policies of the U.S. Geological Survey. Mention of trade names or commercial products does not constitute their endorsement by the U.S. Geological Survey. This work is also supported by the National Science Foundation under Grant No. 1735139.

Author contributions: KW (Data curation [lead], Formal analysis [lead], Investigation [lead], Methodology [equal], Software [equal], Validation [equal], Visualization [lead], Writing – original draft [lead], Writing – review & editing [equal]), DSS (Conceptualization [lead], Formal analysis [supporting], Funding acquisition [lead], Investigation [supporting], Methodology [equal], Project administration [lead], Resources [equal], Supervision [lead], Validation [equal], Writing – review & editing [equal]); JA (Data curation [supporting], Formal analysis [supporting], Investigation [supporting], Methodology [equal], Resources [equal], Software [equal], Writing – review & editing [equal]); SK (Conceptualization [supporting], Investigation [supporting], Methodology [supporting], Writing – review & editing [equal]); and EN (Investigation [supporting], Writing – review & editing [supporting]).

SUPPORTING INFORMATION

Supplementary data are available at *GJI* online.

Figure S1. Pressure, density and gravity magnitude from the surface to the core–mantle boundary applied in all eight model set-ups.

Figure S2. Global present-day instantaneous dynamic topography constrained by temperature model with CBF, without CBF and the residuals.

Figure S3. Global rate of change since 3 Ma of dynamic topography constrained by temperature model with CBF, without CBF and the residuals.

Figure S4. Global present-day instantaneous dynamic topography constrained by the boundary condition with CBF, without CBF and the residuals.

Figure S5. Global rate of change since 3 Ma of dynamic topography constrained by the boundary condition with CBF, without CBF and the residuals.

Figure S6. Present-day instantaneous dynamic topography constrained by the average temperature model over both boundary conditions on the US East Coast with CBF, without CBF and the residuals.

Figure S7. Rate of change since 3 Ma of dynamic topography constrained by the average temperature model over both boundary conditions on the US East Coast with CBF, without CBF and the residuals.

Figure S8. Present-day instantaneous dynamic topography constrained by the average boundary condition over all three temperature models on the US East Coast with CBF, without CBF and the residuals.

Figure S9. Rate of change since 3 Ma of dynamic topography constrained by the average boundary condition over all three temperature models on the US East Coast with CBF, without CBF and the residuals.

Figure S10. Change in dynamic topography over the past 3 million years on the US East Coast for every individual model set-up with and without CBF.

Figure S11. Distribution of change in dynamic topography over 125 k years with and without CBF at global sea level markers from the LIG sea level marker compilation from Austermann *et al.* (2017).

DATA AVAILABILITY

Our code, parameter files, input files and model output files are made available on Zenodo (ASPECT_v2.2.0-Williams_et_al) for reproducibility (Williams *et al.* 2023).

REFERENCES

Auer, L., Boschi, L., Becker, T.W., Nissen-Meyer, T. & Giardini, D., 2014. Savani: a variable resolution whole-mantle model of anisotropic shear velocity variations based on multiple data sets. *J. Geophys. Res.*, **119**(3006–3034. 4).

Austermann, J., Mitrovica, J.X., Huybers, P. & Rovere, A., 2017. Detection of a dynamic topography signal in last interglacial sea-level records. *Sci. Adv.,* **3**(7), e1700457.

Austermann, J., Pollard, D., Mitrovica, J.X., Moucha, R., Forte, A.M., DeConto, R.M., Rowley, D.B. & Raymo, M.E., 2015. The impact of dynamic topography change on Antarctic ice sheet stability during the mid-pliocene warm period. *Geology,* **43**(10), 927–930.

Bangerth, W., Dannberg, J., Gassmoeller, R. & Heister, T. 2020. *ASPECT v2.2.0,* Zenodo.

Baumgardner, J.R., 1985. Three-dimensional treatment of convective flow in the Earth's mantle. *J. Stat. Phys.,* **39,** 501–511.

Bertelloni, C.L. & Gurnis, M., 1997. Cenozoic subsidence and uplift of continents from time-varying dynamic topography. *Geology,* **25**(8), 735–738.

Brezzi, F. & Douglas, J., 1988. Stabilized mixed methods for the Stokes problem. *Numer. Math.,* **53,** 225–235.

Bunge, H.P., Richards, M.A. & Baumgardner, J.R., 1996. Effect of depth-dependent viscosity on the planform of mantle convection. *Nature,* **379**(6564), 436–438.

Burstedde, C., Stadler, G., Alisic, L., Wilcox, L.C., Tan, E., Gurnis, M. & Ghattas, O., 2013. Large-scale adaptive mantle convection simulation. *Geophys. J. Int.,* **192**(3), 889–906.

Choblet, G., Čadek, O., Couturier, F. & Dumoulin, C., 2007. OEDIPUS: a new tool to study the dynamics of planetary interiors. *Geophys. J. Int.,* **170**(1), 9–30.

Conrad, C.P. & Husson, L., 2009. Influence of dynamic topography on sea level and its rate of change. *Lithosphere,* **1**(2), 110–120.

Crameri, F. *et al.* 2012. A comparison of numerical surface topography calculations in geodynamic modelling: an evaluation of the 'sticky air' method. *Geophys. J. Int.,* **189**(1), 38–54.

Dannberg, J. & Heister, T., 2016. Compressible magma/mantle dynamics: 3-D, adaptive simulations in ASPECT. *Geophys. J. Int.,* **207**(3), 1343–1366.

Ding, X., Salles, T., Flament, N., Mallard, C. & Rey, P.F., 2019. Drainage and sedimentary responses to dynamic topography. *Geophys. Res. Lett.,* **46**(24), 14385–14394.

Dziewonski, A.M. & Anderson, D.L., 1981. Preliminary reference Earth model. *Phys. Earth planet. Inter.,* **25**(4), 297–356.

Ern, A. & Guermond, J.L., 2004. Accurate numerical simulation of radiative heat transfer with application to crystal growth. *Int. J. Numer. Methods Eng.,* **61**(4), 559–583.

Flament, N., Gurnis, M. & Müller, R.D., 2013. A review of observations and models of dynamic topography. *Lithosphere,* **5**(2), 189–210.

Forte, A.M. & Rowley, D.B., 2022. Earth's isostatic and dynamic topography—a critical perspective. *Geochem. Geophys. Geosyst.,* **23**(9), e2021GC009740.

Forte, A.M., Moucha, R., Simmons, N.A., Grand, S.P. & Mitrovica, J.X., 2010. Deep-mantle contributions to the surface dynamics of the North American continent. *Tectonophysics,* **481**(1-4), 3–15.

Gassmöller, R., Dannberg, J., Bangerth, W., Heister, T. & Myhill, R., 2020. On formulations of compressible mantle convection. *Geophys. J. Int.,* **221**(2), 1264–1280.

Glišović, P. & Forte, A.M., 2015. Importance of initial buoyancy field on evolution of mantle thermal structure: implications of surface boundary conditions. *Geosci. Front.,* **6**(1), 3–22.

Gurnis, M., 1990. Bounds on global dynamic topography from phanerozoic flooding of continental platforms. *Nature,* **344**(6268), 754–756.

Gurnis, M., Eloy, C. & Zhong, S., 1996. Free-surface formulation of mantle convection—II. Implication for subduction-zone observables. *Geophys. J. Int.,* **127**(3), 719–727.

Hack, J.T., 1975. Dynamic equilibrium and landscape evolution, in Melhorn, W.N., *Theories of Landform Development,* Vol. 1, pp. State University of New York, 87–102.

Hager, B. H. & O'Connell,, R. J., 1981. A simple global model of plate dynamics and mantle convection. *J. geophys. Res.,* **86**(B6), 4843–4867.

Hager, B.H., Clayton, R.W., Richards, M.A., Comer, R.P. & Dziewonski, A.M., 1985. Lower mantle heterogeneity, dynamic topography and the geoid. *Nature,* **313**(6003), 541–545.

Heine, C., Müller, R.D., Steinberger, B. & Torsvik, T.H., 2008. Subsidence in intracontinental basins due to dynamic topography. *Phys. Earth Planet. Inter.,* **171**(1–4), 252–264.

Heister, T., Dannberg, J., Gassmöller, R. & Bangerth, W., 2017. High accuracy mantle convection simulation through modern numerical methods–II: realistic models and problems. *Geophys. J. Int.,* **210**(2), 833–851.

Hoggard, M., Austermann, J., Randel, C. & Stephenson, S., 2021. Observational estimates of dynamic topography through space and time, in Marquardt, H., Ballmer, M., Cottaar, S. & Konter, J., *Mantle Convection and Surface Expressions,* pp. American Geophysical Union 371–411.

Kramer, S.C., Wilson, C.R. & Davies, D.R., 2012. An implicit free surface algorithm for geodynamical simulations. *Phys. Earth planet. Inter.,* **194,** 25–37.

Kronbichler, M., Heister, T. & Bangerth, W., 2012. High accuracy mantle convection simulation through modern numerical methods. *Geophys. J. Int.,* **191**(1), 12–29.

Leng, W. & Zhong, S., 2008. Viscous heating, adiabatic heating and energetic consistency in compressible mantle convection. *Geophys. J. Int.,* **173**(2), 693–702.

Liu, L., 2014. Rejuvenation of Appalachian topography caused by subsidence-induced differential erosion. *Nat. Geosci.,* **7**(7), 518–523.

Liu, L., 2015. The ups and downs of North America: evaluating the role of mantle dynamic topography since the Mesozoic. *Rev. Geophys.,* **53**(3), 1022–1049.

Liu, S. & King, S.D., 2019. A benchmark study of incompressible stokes flow in a 3-D spherical shell using ASPECT. *Geophys. J. Int.,* **217**(1), 650–667.

Lu, C., Grand, S.P., Lai, H. & Garnero, E.J., 2019. TX2019slab: a new P and S tomography model incorporating subducting slabs. *J. geophys. Res.,* **124**(11), 11 549–11 567.

McKenzie, D., 1977. Surface deformation, gravity anomalies and convection. *Geophys. J. Int.,* **48**(2), 211–238.

Mitrovica, J.X. & Forte, A.M., 2004. A new inference of mantle viscosity based upon joint inversion of convection and glacial isostatic adjustment data. *Earth planet. Sci. Lett.,* **225**(1–2), 177–189.

Molnar, P., England, P.C. & Jones, C.H., 2015. Mantle dynamics, isostasy, and the support of high terrain. *J. geophys. Res.,* **120**(3), 1932–1957.

Moucha, R. & Ruetenik, G.A., 2017. Interplay between dynamic topography and flexure along the US Atlantic passive margin: insights from landscape evolution modeling. *Glob. Planet. Change,* **149,** 72–78.

Moucha, R., Forte, A.M., Mitrovica, J.X., Rowley, D.B., Quéré, S., Simmons, N.A. & Grand, S.P., 2008. Dynamic topography and long-term sea-level variations: there is no such thing as a stable continental platform. *Earth planet. Sci. Lett.,* **271**(1-4), 101–108.

Müller, R.D., Hassan, R., Gurnis, M., Flament, N. & Williams, S.E., 2018. Dynamic topography of passive continental margins and their hinterlands since the Cretaceous. *Gondwana Res.,* **53,** 225–251.

Panasyuk, S.V. & Hager, B.H., 2000. Inversion for mantle viscosity profiles constrained by dynamic topography and the geoid, and their estimated errors. *Geophys. J. Int.,* **143**(3), 821–836.

Ratcliff, J.T., Schubert, G. & Zebib, A., 1996. Steady tetrahedral and cubic patterns of spherical shell convection with temperature-dependent viscosity. *J. geophys. Res.,* **101**(B11), 25 473–25 484.

Ritsema, J., Deuss, A., Van Heijst, H.J. & Woodhouse, J.H., 2011. S40RTS: a degree-40 shear-velocity model for the mantle from new Rayleigh wave dispersion, teleseismic traveltime and normal-mode splitting function measurements. *Geophys. J. Int.,* **184**(3), 1223–1236.

Rovere, A., Hearty, P.J., Austermann, J., Mitrovica, J.X., Gale, J., Moucha, R., Forte, A.M. & Raymo, M.E., 2015. Mid-pliocene shorelines of the US Atlantic Coastal Plain—an improved elevation database with comparison to Earth model predictions. *Earth Sci. Rev.,* **145,** 117–131.

Rowley, D.B., Forte, A.M., Moucha, R., Mitrovica, J.X., Simmons, N.A. & Grand, S.P., 2013. Dynamic topography change of the eastern United States since 3 million years ago. *Science,* **340**(6140), 1560–1563.

Ruetenik, G.A., Moucha, R. & Hoke, G.D., 2016. Landscape response to changes in dynamic topography. *Terra Nova,* **28**(4), 289–296.

Schmid, C., Goes, S., Van der Lee, S. & Giardini, D., 2002. Fate of the cenozoic Farallon slab from a comparison of kinematic thermal modeling with tomographic images. *Earth planet. Sci. Lett.,* **204**(1-2), 17–32.

Simmons, N.A., Forte, A.M. & Grand, S.P., 2009. Joint seismic, geodynamic and mineral physical constraints on three-dimensional mantle heterogeneity: implications for the relative importance of thermal versus compositional heterogeneity. *Geophys. J. Int.,* **177**(3), 1284–1304.

Spasojevic, S., Liu, L. & Gurnis, M., 2009. Adjoint models of mantle convection with seismic, plate motion, and stratigraphic constraints: North America since the Late Cretaceous. *Geochem. Geophys. Geosyst.,* **10**(5), 1–24.

Steinberger, B., 2016. Topography caused by mantle density variations: observation-based estimates and models derived from tomography and lithosphere thickness. *Geophys. Suppl. Mon. Not. R. Astron. Soc.,* **205**(1), 604–621.

Stemmer, K., Harder, H. & Hansen, U., 2006. A new method to simulate convection with strongly temperature- and pressure-dependent viscosity in a spherical shell: applications to the Earth's mantle. *Phys. Earth planet. Inter.,* **157**(3-4), 223–249.

Stover, C.W. & Coffman, J.L., 1992. *Seismicity of the United States, 1568-1989 (revised)*. US Government Printing Office.

Tackley, P.J., 1993. Effects of strongly temperature-dependent viscosity on time-dependent, three-dimensional models of mantle convection. *Geophys. Res. Lett.,* **20**(20), 2187–2190.

Williams, K.A., Austermann, J.A., Stamps, D.S., King, S.D. & Njinju, E.A., 2023. *ASPECT_v2.2.0-Williams_et_al [Software],* Zenodo. https://doi.org/10.5281/zenodo.8010805

Yoshida, M. & Kageyama, A., 2004. Application of the Yin-Yang grid to a thermal convection of a Boussinesq fluid with infinite prandtl number in a three-dimensional spherical shell. *Geophys. Res. Lett.,* **31**(12), 1–5.

Zhong, S., Gurnis, M. & Hulbert, G., 1993. Accurate determination of surface normal stress in viscous flow from a consistent boundary flux method. *Phys. Earth planet. Inter.,* **78**(1–2), 1–8.

Zhong, S., Gurnis, M. & Moresi, L., 1996. Free-surface formulation of mantle convection—I. Basic theory and application to plumes. *Geophys. J. Int.,* **127**(3), 708–718.

Zhong, S., McNamara, A., Tan, E. & Moresi, L., 2008. A benchmark study on mantle convection in a 3-D spherical shell using CitcomS. *Geochem. Geophys. Geosyst.,* **9**(10), 1–32.

Zhong, S., Zuber, M.T., Moresi, L. & Gurnis, M., 2000. Role of temperature-dependent viscosity and surface plates in spherical shell models of mantle convection. *J. geophys. Res.,* **105**(B5), 11 063–11 082.